CYSTIC FIBROSIS

Molecular structures reveal synergistic rescue of Δ508 CFTR by Trikafta modulators

Karol Fiedorczuk[1] and Jue Chen[1,2]*

The predominant mutation causing cystic fibrosis, a deletion of phenylalanine 508 (Δ508) in the cystic fibrosis transmembrane conductance regulator (CFTR), leads to severe defects in CFTR biogenesis and function. The advanced therapy Trikafta combines the folding corrector tezacaftor (VX-661), the channel potentiator ivacaftor (VX-770), and the dual-function modulator elexacaftor (VX-445). However, it is unclear how elexacaftor exerts its effects, in part because the structure of Δ508 CFTR is unknown. Here, we present cryo–electron microscopy structures of Δ508 CFTR in the absence and presence of CFTR modulators. When used alone, elexacaftor partially rectified interdomain assembly defects in Δ508 CFTR, but when combined with a type I corrector, did so fully. These data illustrate how the different modulators in Trikafta synergistically rescue Δ508 CFTR structure and function.

Cystic fibrosis (CF) is a common genetic disease (*1*) caused by mutations in the gene that encodes the cystic fibrosis transmembrane conductance regulator (CFTR) (*2*, *3*). CFTR is widely expressed in epithelial cells, regulating salt and fluid homeostasis in a variety of tissues. The absence or dysfunction of CFTR causes health issues, including malnutrition, liver disease, recurrent bacterial infection, chronic inflammation, and respiratory failure (*4*).

CFTR belongs to the ATP-binding cassette (ABC) transporter family but functions as an ATP-gated anion channel (*5*–*7*). It contains an N-terminal interfacial structure called the lasso motif, two transmembrane domains (TMDs) that form an anion conduction pathway, two cytoplasmic nucleotide-binding domains (NBDs) that bind and hydrolyze ATP (*8*), and a unique regulatory (R) domain that must be phosphorylated to open the channel (*9*, *10*). Although >300 mutations cause CF, ~90% of patients carry at least one copy of Δ508 CFTR in which a single phenylalanine at position 508 is deleted (*11*, *12*). This Δ508 mutant exhibits a severe trafficking defect that results in intracellular retention and premature degradation of the channel (*13*). Furthermore, the few channels that reach the plasma membrane are unstable and functionally compromised (*14*–*16*).

The structure of wild-type (WT) CFTR shows that F508 resides on the surface of NBD1, where it makes extensive interactions with the cytosolic region of TM helix 11 and intracellular loop 4 (*8*, *17*). These interactions are critical for both CFTR folding and coupling of ATP-dependent NBD dimerization to pore opening (*18*), suggesting that disruption of these interactions may underlie both trafficking and functional defects in Δ508 CFTR. Indeed, a previous crystal structure of an isolated NBD1 containing Δ508 revealed a conformation nearly identical to WT NBD1 (*19*), supporting the hypothesis that Δ508 primarily affects interdomain assembly (*8*, *19*–*22*). Other studies have shown that a lack of F508 causes thermodynamic instability of NBD1 and the entire CFTR protein (*20*, *23*). Unfortunately, the intrinsic instability of Δ508 CFTR has hindered efforts to structurally characterize the mutant in the context of the entire CFTR protein.

Despite these structural obstacles, recently developed CFTR modulators have transformed CF therapy from symptom management to disease correction. These modulators include potentiators that enhance the function of CFTR in the plasma membrane and correctors that increase the abundance of CFTR at the cell surface (*24*, *25*). CFTR correctors are further categorized into three different classes on the basis of their functional redundancy (*26*, *27*). Currently, there are four pharmacological molecules used in CF therapy, either singly or in combination. These include the potentiator ivacaftor (VX-770), the type I correctors lumacaftor (VX-809) and tezacaftor (VX-661), and the type III corrector elexacaftor (VX-445) (Fig. 1A). The most advanced therapy, Trikafta (branded as Kaftrio in Europe) is a combination of ivacaftor, tezacaftor, and elexacaftor. The molecular mechanisms of ivacaftor and type I correctors have been well studied (*28*, *29*). Elexacaftor, however, was discovered only recently and little is known about its mode of action. It has been shown to have a dual function, improving CFTR folding as well as ion conductance (*27*, *30*–*33*), but it is unknown whether it potentiates and corrects through the same binding site.

In this study, we determined cryo–electron microscopy (cryo-EM) structures of Δ508 CFTR and analyzed the molecular effects of lumacaftor, tezacaftor, and elexacaftor, revealing how elexacaftor might potentiate the activity of Δ508 and stabilize its structure. We also solved the structure of Δ508 CFTR in the presence of the three modulators comprising the triple therapy, providing a molecular description of how they synergistically rectify Δ508 CFTR to a functional state.

Δ508 CFTR exhibits defective NBD assembly

We sought to determine the molecular structure of Δ508 CFTR to investigate the mechanisms underlying its trafficking defect and gating deficiency. For WT CFTR (*29*, *34*, *35*), substituting the catalytic residue E1371 with a glutamine was necessary to stabilize an ATP-bound, NBD-dimerized conformation for the cryo-EM study. To test whether E1371Q alters the folding of Δ508 CFTR both with and without pharmacological correctors, we used a gel-shift assay to quantify the relative abundance of the fully glycosylated mature protein relative to the core-glycosylated immature form (*36*). In the absence of correctors, Δ508 and Δ508/E1371Q CFTR were predominantly in their immature form (core-glycosylated, lower molecular weight). The addition of correctors increased the abundance of the mature forms (fully glycosylated, higher molecular weight) for both variants to a similar extent (Fig. 1B). Confocal microscopy confirmed that Δ508 and Δ508/E1371Q CFTR were retained in the endoplasmic reticulum (ER), and that correctors increased their presence at the plasma membrane (Fig. 1C and fig. S1). These data demonstrate that, similar to Δ508 CFTR, the double mutant Δ508/E1371Q exhibits folding defects that can be reverted by correctors.

Next, we purified the ER-retained Δ508/E1371Q CFTR without any pharmacological correctors (fig. S2) and determined its structure in the absence and presence of phosphorylation and ATP (Fig. 1D). In both conditions, the flexibility of NBD1 became apparent in the initial two-dimensional (2D) classification steps of data processing (fig. S3). After extensive 3D classification, the structure of the dephosphorylated, ATP-free form was determined at ~6-Å resolution (Fig. 1D and fig. S3), revealing an NBD-separated conformation similar to that of WT CFTR (*8*, *17*). Densities corresponding to the TM helices and NBD2 revealed well-defined secondary structural features. The density for NBD1 was visible but amorphous, with a size and shape consistent with that of NBD1, indicating that Δ508 NBD1 is folded but flexibly attached to the TM helices. This structural observation supports the hypothesis that Δ508 disrupts interdomain assembly (*8*, *19*–*22*). In contrast to WT CFTR, in which the structured R domain inserts into a cytosolic cleft (*8*, *17*), little density corresponding to the R domain was visible in Δ508 CFTR. Because the R domain packs mainly along the surface of NBD1, it is possible

[1]Laboratory of Membrane Biology and Biophysics, The Rockefeller University, New York, NY 10065, USA. [2]Howard Hughes Medical Institute, Chevy Chase, MD 20815, USA.
*Corresponding author. Email: juechen@rockefeller.edu

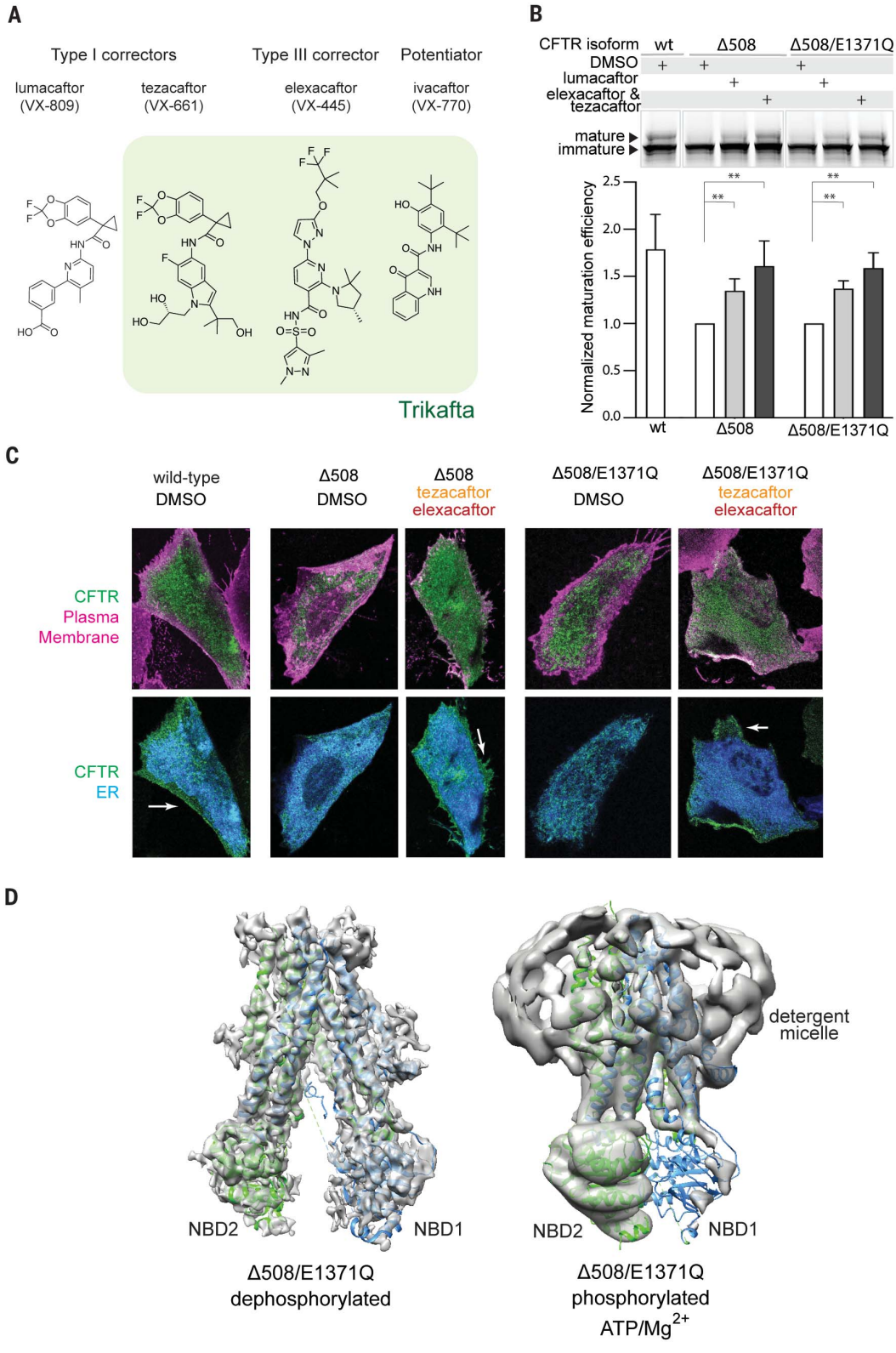

Fig. 1. Δ508 CFTR exhibits defective NBD assembly. (**A**) Four CFTR modulators currently used in the clinical setting. Green highlights the composition of the triple therapy (Trikafta in the United States and Kaftrio in Europe). (**B**) Maturation assay in human embryonic kidney 293F (HEK293F) cells. Top panel: SDS–polyacrylamide gel electrophoresis (SDS-PAGE) of cell lysates; mature and immature CFTR were visualized with a C-terminal green fluorescent protein (GFP) tag. Bottom panel: Quantification of $n = 3$ to 6 biological repeats. SDs are indicated by error bars. Concentrations were as follows: lumacaftor, 1 μM; tezacaftor, 10 μM; and elexacaftor, 0.5 μM in 0.1% dimethylsulfoxide (DMSO). Statistical significance was calculated using paired t test. $^{**}0.001 < P < 0.01$. (**C**) Confocal laser scanning microscopy analysis. Chinese hamster ovary (CHO) cells expressing CFTR variants were treated with DMSO (control) or 10 μM tezacaftor and 0.5 μM elexacaftor. ER (blue) was visualized by exciting mCherry-tagged tapasin. Plasma membrane (magenta) was visualized by exciting Alexa Fluor 647–conjugated wheat germ agglutinin stain. CFTR (green) was visualized by exciting enhanced GFP (eGFP)–tagged CFTR. (**D**) Structures of dephosphorylated and phosphorylated, ATP-bound Δ508/E1371Q CFTR. Cryo-EM maps (gray) are superposed with structures of WT CFTR in the same conditions (dephosphorylated PDB, 7SVR; phosphorylated, ATP-bound PDB, 7SVD).

that defects in NBD1 assembly also disrupt its correct positioning.

The lack of structural stability in Δ508 CFTR was even more pronounced in the phosphorylated, ATP-bound conformation. Previous structures of WT, phosphorylated, and ATP-bound CFTR carrying the same E1371Q mutation were determined to resolutions between 2.7 and 3.8 Å (*29*, *34*, *35*). However, the analogous cryo-EM analysis of Δ508 CFTR stalled at ~9-Å resolution because of the heterogeneous nature of the particles (Fig. 1D and fig. S2). The overall structure is consistent with an NBD-dimerized conformation, but a notable difference is the absence of visible density

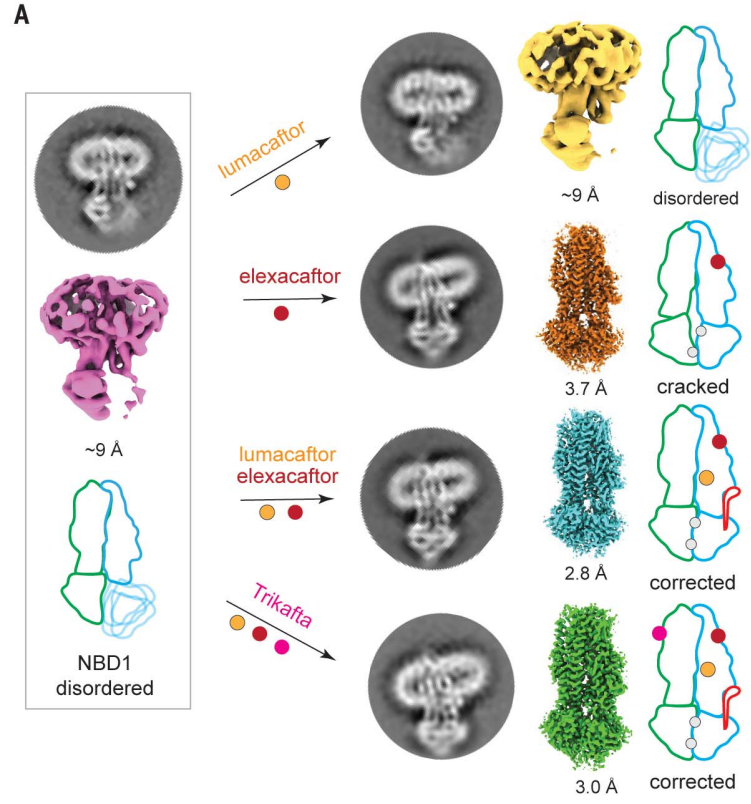

Fig. 2. Conformational changes induced by correctors in Δ508 CFTR. (**A**) Summary of structural analysis of Δ508/E1371Q CFTR in the absence and presence of correctors. Average projection from 2D classification, final 3D reconstruction, and schematic representation are shown for each structure. NBD1 and TMD1 are shown in blue, NBD2 and TMD2 in green, the R domain in red, ATP as a gray dot, and CFTR modulators as colored dots. (**B** to **D**) Structures of Δ508/E1371Q CFTR in complex with modulators. Top left panels show the overall structures. Top right panels show Cα displacements of the Δ508/E1371Q compared with the WT/E1371Q CFTR (PDB, 7SVD). Bottom left panels are zoomed-in views of the Δ508 NBD dimer. Bottom right panels are superpositions of the NBD structures of Δ508 (NBD1, blue; NBD2, green) and WT CFTR (gray). Drug molecules are represented as sphere models.

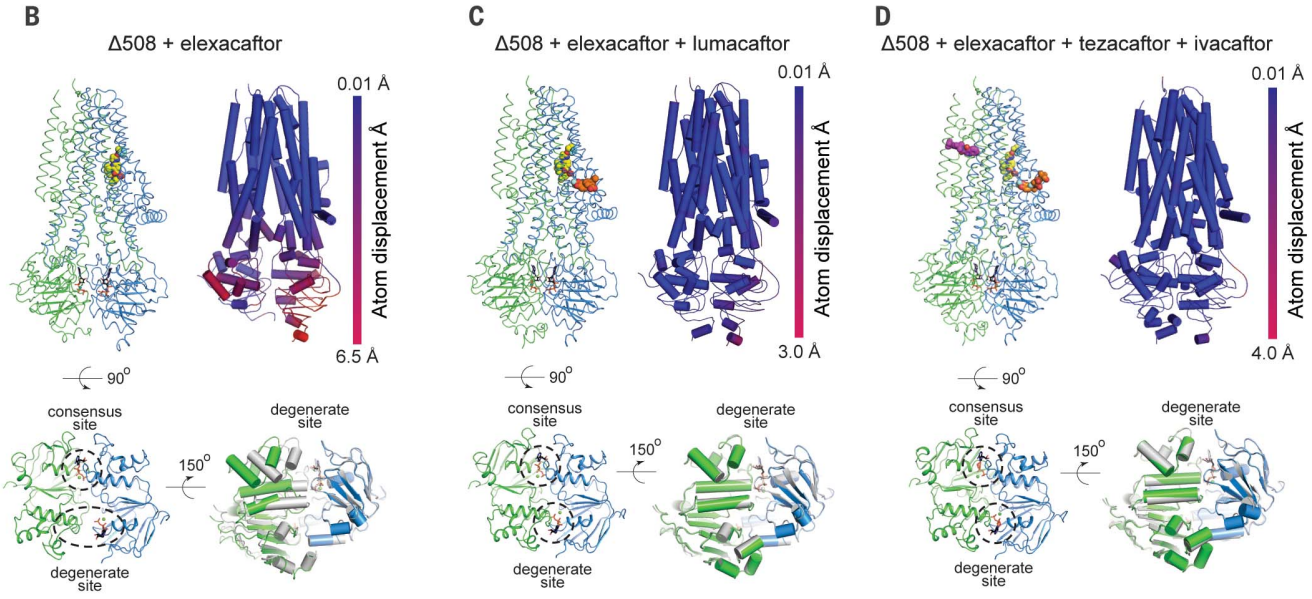

corresponding to NBD1 (Fig. 1D and fig. S3). On the basis of these data, we suggest that the R domain disengages upon phosphorylation as it does in the WT protein, permitting the TMDs to come into close contact. However, in the absence of F508, NBD1 is too flexible to support a stable NBD dimer. Because NBD dimerization is coupled to channel gating in CFTR (*37*), the inability of the NBDs to dimerize in Δ508 explains its impaired channel function (*14–16*, *38*).

Correctors restore NBD dimerization in Δ508 CFTR

To investigate the conformational changes that CFTR correctors induce, we performed cryo-EM analyses of phosphorylated, ATP-bound Δ508/E1371Q CFTR in four pharmacological conditions: (i) lumacaftor, (ii) elexacaftor, (iii) a combination of these two correctors, and (iv) the triple Trikafta therapy of ivacaftor, tezacaftor, and elexacaftor (Fig. 2 and figs. S2 and S3). The Δ508/E1371Q CFTR was expressed in the absence of correctors and solubilized from the ER membrane. Correctors were added during protein purification (fig. S2) to reveal their posttranslational effects on the structure of Δ508 CFTR without any confounding effects on folding kinetics and other cellular processes involved in Δ508 biogenesis.

The structure of Δ508 CFTR in the presence of lumacaftor was similar to that in its absence, indicating that posttranslational addition of lumacaftor alone is insufficient

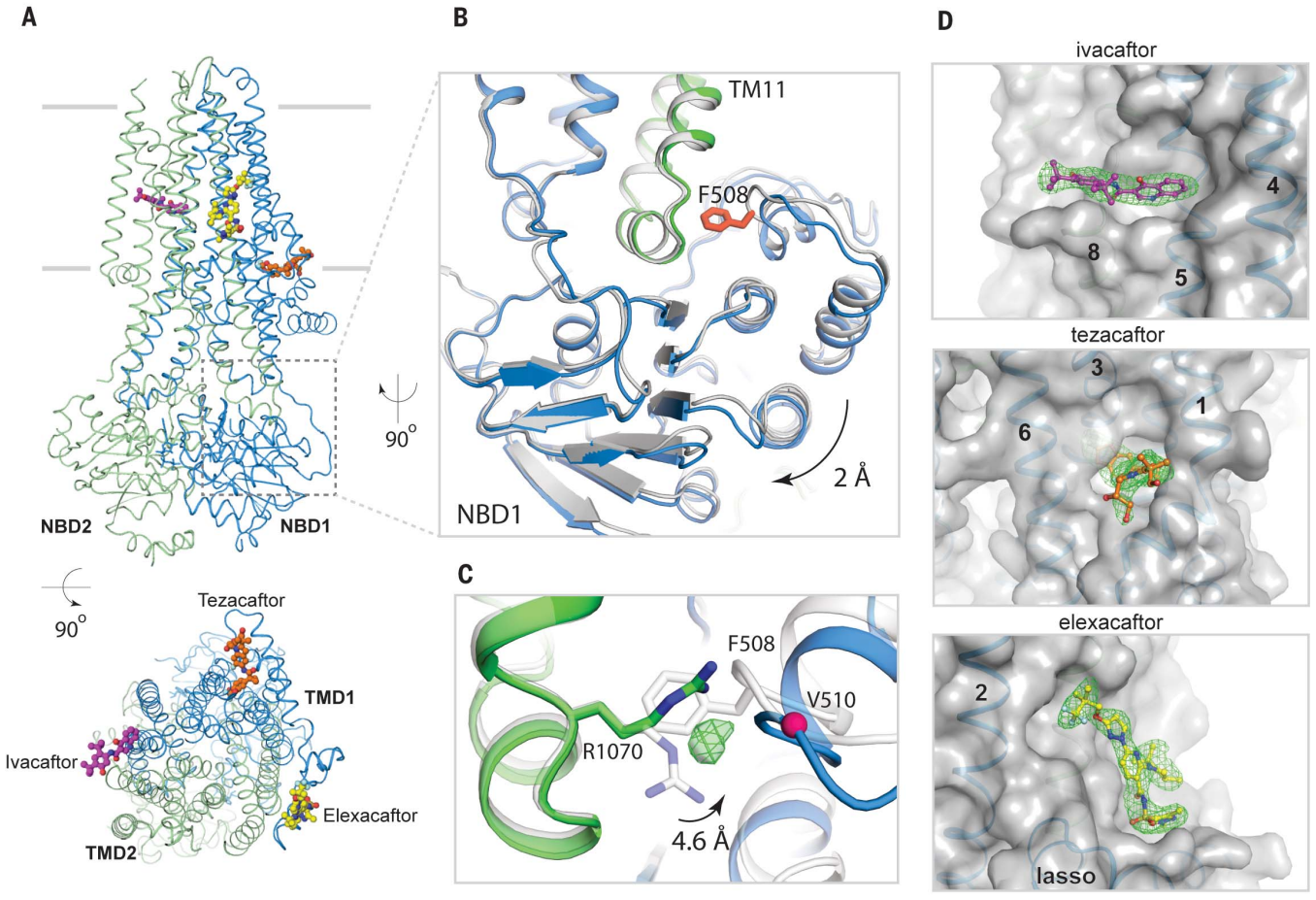

Fig. 3. Structure of Trikafta-corrected Δ508 CFTR. (**A**) Orthogonal views of Δ508/E1371Q CFTR in complex with ivacaftor, elexacaftor, and tezacaftor. Shown is a Δ508 CFTR ribbon diagram with ball-and-stick models of drug molecules. Membrane location is indicated by two gray lines. (**B**) Zoomed-in view of F508 site. The Δ508 CFTR structure (blue/green) is superimposed with the WT CFTR structure (gray). F508 is highlighted in red. (**C**) R1070 conformational change. Unassigned density is shown as a green mesh. (**D**) Zoomed-in views of drug-binding sites. Drug densities are shown as a green mesh, CFTR is shown as a transparent surface model, and the TM helices and lasso motif are labeled.

to correct the structural defects of Δ508 (Fig. 2A). This observation is consistent with the understanding that type I correctors bind to and stabilize TMD1 at an early stage of CFTR biogenesis, preventing its premature degradation and increasing the overall probability of fully folded CFTR being formed (*29*, *39*, *40*).

By contrast, the type III corrector elexacaftor stabilized NBD1, resulting in a cryo-EM reconstruction of 3.7-Å resolution with ordered NBDs (Fig. 2, A and B). The TMDs of elexacaftor-bound Δ508 CFTR closely resemble those of WT/E1371Q CFTR in the phosphorylated, ATP-bound conformation (*35*), but the NBDs are very different (Fig. 2B). Elexacaftor-bound Δ508 has a "cracked-open" NBD dimer in which the catalysis-incompetent (degenerate) site is solvent accessible, and ATP makes contacts exclusively with the NBD1 face of the composite site (Fig. 2B).

The combination of elexacaftor and lumacaftor had an effect that was greater than the sum of each corrector alone, fully restoring Δ508 to an NBD-dimerized conformation with ATP fully occluded both the consensus and degenerate sites (Fig. 2, A and C). Moreover, this structure is essentially identical to that obtained in the presence of Trikafta (Fig. 2A), indicating that ivacaftor does not induce further conformational changes. This is consistent with ivacaftor being a potentiator, not a corrector. Both structures closely resemble that of WF CFTR, having an overall root mean square deviation to the WT protein of 0.5 Å over 1090 Cα positions (Fig. 2, C and D). We therefore designated both elexacaftor plus lumacaftor and Trikafta-bound Δ508 CFTR structures as having a "corrected" conformation and selected Trikafta-bound Δ508 for further analysis.

Pharmacologically corrected Δ508 CFTR has a modified NBD1/TMD interface

The corrected Δ508 structure in the presence of Trikafta differs from that of WT CFTR in the region of the F508 deletion site (Fig. 3, A to C). F508 is located in a loop on the surface of NBD1, projecting its aromatic side chain into a hydrophobic pocket at the end of TM helix 11 (Fig. 3B). Deletion of F508 shortens this loop, leaving a crevice at the NBD1/TMD interface. In addition, the helical subdomain of Δ508 NBD1 (residues 500 to 564) is shifted away from the interface by ~2 Å (Fig. 3B). The crevice at the NBD1/TMD interface is partially filled by R1070, the side chain of which swings into contact with main chain atoms in NBD1 (Fig. 3C). We also observed a strong spherical density in the Δ508 cavity area, which may be an ion or a water molecule.

Previous work has shown that the V510D mutation can stabilize Δ508 CFTR, likely due to aspartic acid forming a salt bridge with R1070 (*41*). The structure of Δ508 is compatible with a salt bridge between these residues and thus lends support to this hypothesis (fig. S4A). The structural differences at the NBD1/TMD interface also explain the opposing

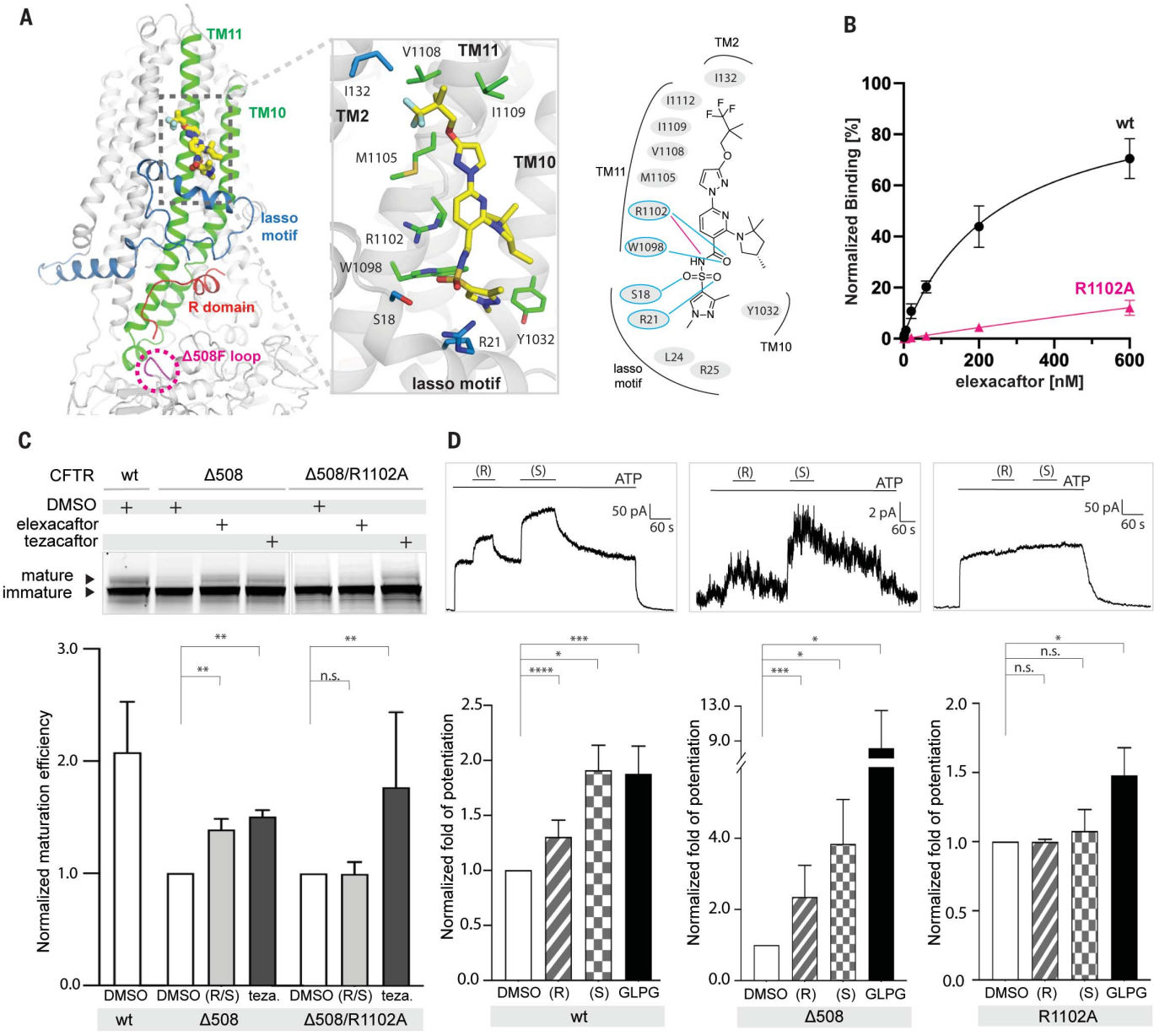

Fig. 4. Elexacaftor binding site. (**A**) Molecular structure of elexacaftor binding site. Left panel is a ribbon diagram. Middle panel is a zoomed-in view of the molecular interactions. Residues within 4.5 Å of elexacaftor are shown as stick models. Right panel is a schematic of the molecular interactions. The salt bridge is shown as a magenta line, and hydrogen bonds are shown as blue lines. (**B**) Quantitative measurement of elexacaftor binding. Data points represent mean and SD for n = 6 to 12 technical repeats (n = 3 to 4 biological repeats). The apparent dissociation constant (K_d) of elexacaftor for WT CFTR is 244 ± 50 nM. (**C**) R1102A mutation diminishes correction by elexacaftor. Top: SDS-PAGE of cell lysates. Bottom: Quantification of n = 3 biological repeats. R/S, racemic mixture of elexacaftor (0.5 μM); Teza, tezacaftor (10 μM). (**D**) Elexacaftor potentiation. Top: Representative macroscopic current traces of fully phosphorylated WT and mutant CFTR in inside-out CHO cell membrane patches. Bottom: Quantification of n = 3 to 8 biological repeats. Concentrations used were as follows: ATP, 3 mM; elexacaftor, 1 μM; and GLPG1837, 10 μM. Fold potentiation was normalized to currents with 3 mM ATP in the absence of potentiators. Statistical significance was calculated using paired t test. n.s., not significant; *P < 0.05; **P < 0.01; ***P < 0.001; ****P < 0.0001.

effects of the R1070W mutation in WT versus Δ508 CFTR. In WT CFTR, substituting R1070 with tryptophan inhibits protein folding and leads to CF (*20*, *42*, *43*). This is because the large tryptophan side chain at position 1070 sterically clashes with F508 (fig. S4B). By contrast, the same substitution in the Δ508 background partially restores CFTR folding (*20*, *22*, *41*, *43*, *44*), likely due to R1070W strengthening the NBD1/TMD interface by filling the space devoid of F508 and forming hydrophobic and hydrophilic contacts with Δ508 NBD1 (fig. S4C).

Trikafta modulators bind to distinct sites on Δ508 CFTR

In the cryo-EM reconstruction of Trikafta-bound Δ508 CFTR, the densities for ivacaftor, tezacaftor, and elexacaftor were strong and unambiguous (Fig. 3). Viewed from the extracellular space perpendicular to the membrane, these compounds form a triangular belt encircling the TMDs (Fig. 3A). The potentiator ivacaftor (Fig. 3, purple molecule) binds to a cleft formed by TM helices 4, 5, and 8 approximately halfway through the lipid bilayer, coincident with the TM helix 8 hinge

region involved in gating (*28*). The molecular details of ivacaftor binding are identical to those in WT CFTR (*28*), indicating that ivacaftor potentiates both WT and Δ508 CFTR through the same mechanism. Similarly, tezacaftor (Fig. 3, orange molecule) binds to Δ508 by inserting into a hydrophobic pocket in TMD1 (Fig. 3D) in a manner identical to that in the WT protein (*29*). As previously discussed, such a penetrating cavity would cause substantial destabilization of the protein in the absence of tezacaftor (*29*). Furthermore, TM helices 1, 2, 3, and 6, which form the binding site, are predicted to be unstable in the membrane, so type I correctors would stabilize TMD1 both by filling the cavity and by structurally linking together the four unstable helices (*29*).

By contrast, the binding site for elexacaftor has not been observed previously. Densities corresponding to elexacaftor are very similar and well defined in the three elexacaftor-bound reconstructions (elexacaftor alone, elexacaftor plus lumacaftor, and Trikafta), enabling an accurate description of elexacaftor's binding pose and the chemistry of drug recognition (fig. S5A). Elexacaftor (Fig. 3, yellow molecule) binds to CFTR within the membrane, extending from the center of the lipid bilayer to the edge of the inner leaflet (Fig. 4A). The binding pocket is much shallower than that of type I correctors as if the drug molecule were patched onto the surface of CFTR. Elexacaftor interacts most extensively with TM helix 11 through electrostatic and van der Waals interactions. It also forms contacts with TM helices 2 and 10 and the lasso motif (Fig. 4A and fig. S5B).

Studies of ivacaftor binding to CFTR have shown that hydrogen bonds are critical for drug recognition because they stabilize polar groups in the low dielectric environment of the membrane (*28*). To determine whether this principle applies to elexacaftor binding, we substituted R1102 with an alanine to eliminate the formation of a hydrogen bond and a salt bridge (Fig. 4A) and then directly measured binding using a scintillation proximity assay (Fig. 4B). Specific binding of elexacaftor to WT CFTR increased as a function of drug concentration. Conversely, the interaction of elexacaftor with the R1102A mutant was barely detectable. We also evaluated the contribution of R1102 to the restoration of Δ508 folding by elexacaftor using the gel-shift assay (Fig. 4C). The R1102A mutation abolished correction by elexacaftor, but not tezacaftor, which binds to a pocket distant from R1102. Finally, to determine whether R1102 also contributes to the potentiation activity of elexacaftor, we measured macroscopic current in inside-out membrane patches containing phosphorylated CFTR (Fig. 4D). We consistently observed stronger potentiation by the S enantiomer in both WT and Δ508 CFTR, in agreement with the higher efficacy of the S enantiomer observed in prior work (*45*). However, R1102A CFTR did not respond to either the R or the S enantiomer, indicating that both enantiomers bind to the site identified in the structures. A control potentiator, GLPG1837, increased macroscopic current in all CFTR variants (Fig. 4D). Together, these data suggest that elexacaftor achieves both correction and potentiation through the same binding site.

Discussion

The structures of Δ508 CFTR reveal that the absence of F508 disrupts the ability of NBD1 to assemble with the TM helices, which leads to intracellular retention and degradation of the protein (*14*, *20*, *46*). Furthermore, the inability to form a stable NBD dimer after phosphorylation and ATP binding results in a dysfunctional channel, even if Δ508 CFTR reaches the plasma membrane (*14*). Pharmacological correctors used in the clinical setting, even added during protein purification, can partially or fully restore the NBD-dimerized conformation. These correctors can improve the folding of WT CFTR and disease-causing mutations (*47*–*51*). Although it is theoretically possible that correctors salvage the different mutant and WT forms of CFTR by entirely different mechanisms, it is likely that their mechanism of action is the same in all cases. Indeed, lumacaftor binds to Δ508 CFTR and WT CFTR at the same site and by interacting with the same residues. Likewise, ivacaftor interacts with WT and Δ508 CFTR in an identical manner, indicating that its mechanism of potentiation is the same for both WT and mutant CFTR.

The dual-function modulator elexacaftor engages TM helices 10 and 11 and the lasso motif, all of which are important for CFTR folding and function. Mutations in the lasso motif can cause intracellular retention or abnormal gating, and some lead to CF (*52*–*59*). TM helices 10 and 11 are the "domain-swapped" helices of TMD2 that extend into the cytosol and interact with NBD1. This interface is important, not only for protein assembly, but also for transmitting conformational changes of the NBDs to the TMDs to control ion permeation. Although the details of how elexacaftor potentiates CFTR await incisive electrophysiology measurements, our structural observations indicate that elexacaftor stabilizes TM helices 10 and 11, thereby strengthening the TMD/NBD1 interface, which is particularly vulnerable to disease-causing mutations (*60*).

Recently, Braakman and colleagues demonstrated that CFTR folding occurs in a stepwise manner (*60*). It is likely that the type I corrector tezacaftor binds at an early stage of CFTR biogenesis to stabilize the N-terminal TMD1 (*29*), and the type III corrector elexacaftor binds at a later stage when TMDs assemble to form a protease-resistant form. Together, these two correctors prevent premature degradation in the ER. Once CFTR reaches the plasma membrane, the presence of elexacaftor strengthens allosteric communication between ATP-bound NBD dimers and the channel gate, thereby increasing ion conductance. Channel activity is further enhanced by ivacaftor, which stabilizes the open configuration of the pore (*28*). In this manner, the three modulators in the triple therapy act synergistically to improve the folding and function of CFTR.

REFERENCES AND NOTES

1. M. Shteinberg, I. J. Haq, D. Polineni, J. C. Davies, *Lancet* **397**, 2195–2211 (2021).
2. B. Kerem *et al*., *Science* **245**, 1073–1080 (1989).
3. J. R. Riordan *et al*., *Science* **245**, 1066–1073 (1989).
4. D. B. Sanders, A. K. Fink, *Pediatr. Clin. North Am.* **63**, 567–584 (2016).
5. M. P. Anderson *et al*., *Cell* **67**, 775–784 (1991).
6. M. P. Anderson, D. P. Rich, R. J. Gregory, A. E. Smith, M. J. Welsh, *Science* **251**, 679–682 (1991).
7. M. L. Drumm *et al*., *Cell* **62**, 1227–1233 (1990).
8. Z. Zhang, J. Chen, *Cell* **167**, 1586–1597.e9 (2016).
9. F. S. Seibert *et al*., *Biochim. Biophys. Acta* **1461**, 275–283 (1999).
10. L. S. Ostedgaard, O. Baldursson, M. J. Welsh, *J. Biol. Chem.* **276**, 7689–7692 (2001).
11. M. D. Amaral, C. M. Farinha, *Curr. Pharm. Des.* **19**, 3497–3508 (2013).
12. J. R. Riordan, *Annu. Rev. Biochem.* **77**, 701–726 (2008).
13. S. H. Cheng *et al*., *Cell* **63**, 827–834 (1990).
14. W. Dalemans *et al*., *Nature* **354**, 526–528 (1991).
15. G. L. Lukacs *et al*., *J. Biol. Chem.* **268**, 21592–21598 (1993).
16. M. Sharma, M. Benharouga, W. Hu, G. L. Lukacs, *J. Biol. Chem.* **276**, 8942–8950 (2001).
17. F. Liu, Z. Zhang, L. Csanády, D. C. Gadsby, J. Chen, *Cell* **169**, 85–95.e8 (2017).
18. P. Vergani, S. W. Lockless, A. C. Nairn, D. C. Gadsby, *Nature* **433**, 876–880 (2005).
19. H. A. Lewis *et al*., *J. Biol. Chem.* **280**, 1346–1353 (2005).
20. W. M. Rabeh *et al*., *Cell* **148**, 150–163 (2012).
21. K. Du, M. Sharma, G. L. Lukacs, *Nat. Struct. Mol. Biol.* **12**, 17–25 (2005).
22. L. He *et al*., *FASEB J.* **24**, 3103–3112 (2010).
23. L. He *et al*., *J. Mol. Biol.* **427**, 106–120 (2015).
24. S. M. Rowe, A. S. Verkman, *Cold Spring Harb. Perspect. Med.* **3**, a009761 (2013).
25. A. Zaher, J. ElSaygh, D. Elsori, H. ElSaygh, A. Sanni, *Cureus* **13**, e16144 (2021).
26. T. Okiyoneda *et al*., *Nat. Chem. Biol.* **9**, 444–454 (2013).
27. G. Veit *et al*., *JCI Insight* **5**, e139983 (2020).
28. F. Liu *et al*., *Science* **364**, 1184–1188 (2019).
29. K. Fiedorczuk, J. Chen, *Cell* **185**, 158–168.e11 (2022).
30. D. Keating *et al*., *N. Engl. J. Med.* **379**, 1612–1620 (2018).
31. G. Veit, C. Vaccarin, G. L. Lukacs, *J. Cyst. Fibros.* **20**, 895–898 (2021).
32. C. A. Shaughnessy, P. L. Zeitlin, P. E. Bratcher, *Sci. Rep.* **11**, 19810 (2021).
33. O. Laselva *et al*., *Eur. Respir. J.* **57**, 2002774 (2021).
34. Z. Zhang, F. Liu, J. Chen, *Cell* **170**, 483–491.e8 (2017).
35. Z. Zhang, F. Liu, J. Chen, *Proc. Natl. Acad. Sci. U.S.A.* **115**, 12757–12762 (2018).
36. X. B. Chang *et al*., *J. Cell Sci.* **121**, 2814–2823 (2008).
37. L. Csanády, P. Vergani, D. C. Gadsby, *Physiol. Rev.* **99**, 707–738 (2019).
38. K. Y. Jih, M. Li, T. C. Hwang, S. G. Bompadre, *J. Physiol.* **589**, 2719–2731 (2011).
39. T. W. Loo, M. C. Bartlett, D. M. Clarke, *Biochem. Pharmacol.* **86**, 612–619 (2013).
40. B. Kleizen *et al*., *J. Mol. Biol.* **433**, 166955 (2021).
41. T. W. Loo, M. C. Bartlett, D. M. Clarke, *Biochemistry* **49**, 6352–6357 (2010).
42. K. V. Krasnov, M. Tzetis, J. Cheng, W. B. Guggino, G. R. Cutting, *Hum. Mutat.* **29**, 1364–1372 (2008).
43. J. L. Mendoza *et al*., *Cell* **148**, 164–174 (2012).
44. P. H. Thibodeau *et al*., *J. Biol. Chem.* **285**, 35825–35835 (2010).

45. V. Capurro *et al.*, *Int. J. Mol. Sci.* **22**, 5262 (2021).
46. H. Hoelen *et al.*, *PLOS ONE* **5**, e15458 (2010).
47. F. Van Goor *et al.*, *Proc. Natl. Acad. Sci. U.S.A.* **108**, 18843–18848 (2011).
48. G. L. Lukacs, A. S. Verkman, *Trends Mol. Med.* **18**, 81–91 (2012).
49. S. Moniz *et al.*, *ACS Chem. Biol.* **8**, 432–442 (2013).
50. L. He *et al.*, *FASEB J.* **27**, 536–545 (2013).
51. H. Y. Ren *et al.*, *Mol. Biol. Cell* **24**, 3016–3024 (2013).
52. A. P. Naren, M. W. Quick, J. F. Collawn, D. J. Nelson, K. L. Kirk, *Proc. Natl. Acad. Sci. U.S.A.* **95**, 10972–10977 (1998).
53. A. P. Naren *et al.*, *Science* **286**, 544–548 (1999).
54. L. S. Prince *et al.*, *J. Biol. Chem.* **274**, 3602–3609 (1999).
55. K. W. Peters, J. Qi, J. P. Johnson, S. C. Watkins, R. A. Frizzell, *Pflugers Arch.* **443**, S65–S69 (2001).
56. F. Bilan *et al.*, *J. Cell Sci.* **117**, 1923–1935 (2004).
57. A. Jurkuvenaite *et al.*, *J. Biol. Chem.* **281**, 3329–3334 (2006).
58. G. G. Gené *et al.*, *Hum. Mutat.* **29**, 738–749 (2008).
59. J. Fu, H. L. Ji, A. P. Naren, K. L. Kirk, *J. Physiol.* **536**, 459–470 (2001).
60. J. Im *et al.*, ABC-transporter CFTR folds with high fidelity through a modular, stepwise pathway. bioRxiv 500765 [Preprint] (2022); https://doi.org/10.1101/2022.07.20.500765.

ACKNOWLEDGMENTS

We thank M. Ebrahim, H. Ng, and J. Sotiris at Rockefeller's Evelyn Gruss Lipper Cryo-Electron Microscopy Resource Center for assistance in electron microscopy data collection; F. Glickman of the Rockefeller High Throughput and Spectroscopy Resource Center for help with the scintillation proximity assay experiments; P. Banerjee at the Frits and Rita Markus Bio-Imaging Resource Center at The Rockefeller University for assistance in confocal microscopy data collection; J. Levring from the Laboratory of Membrane Biology and Biophysics for assistance in electrophysiology recordings; and D. Tallent for proofreading the manuscript.
Funding: This work was supported by the Howard Hughes Medical Institute (J.C.) and the Cystic Fibrosis Foundation Therapeutics (J.C. and K.F.). **Author contributions:** K.F. performed all of the experiments. K.F. and J.C. conceptualized the study, analyzed the data, and wrote the manuscript. **Competing interests:** The authors declare no competing interests. **Data and materials availability:** Protein models and cryo-EM maps are available at the RCSB Protein Data Bank (https://www.rcsb.org/) and the Electron Microscopy Data Bank (https://www.ebi.ac.uk/emdb/), respectively, under codes 8EJ1 and EMD-28172 (dephosphorylated Δ508/E1371Q), 8EIG and EMD-28155 (phosphorylated Δ508/E1371Q with ATP/Mg^{2+}/elexacaftor), 8EIO and EMD-28160 (phosphorylated Δ508/E1371Q with ATP/Mg^{2+}/elexacaftor/lumacaftor), and 8EIQ and EMD-28161 (phosphorylated Δ508/E1371Q with ATP/Mg^{2+}/Trikafta). All other data and information are available in the main text or the supplementary materials.

SUPPLEMENTARY MATERIALS

science.org/doi/10.1126/science.ade2216
Materials and Methods
Figs. S1 to S5
Table S1
References (*61*–*71*)
MDAR Reproducibility Checklist

View/request a protocol for this paper from *Bio-protocol*.

Submitted 1 August 2022; accepted 27 September 2022
10.1126/science.ade2216